Microsyst Technol (2017) 23:441–456
DOI 10.1007/s00542-016-3048-3

TECHNICAL PAPER

Design and analysis of a compliant micro-positioning platform with embedded strain gauges and viscoelastic damper

Thanh-Phong Dao[1,2] · Shyh-Chour Huang[3]

Received: 19 March 2016 / Accepted: 21 June 2016 / Published online: 27 June 2016
© Springer-Verlag Berlin Heidelberg 2016

Abstract Compliant micro-positioning platforms are necessary for highly precise applications. Measurements of the displacement and reinforcements of the stiffness are two major concerns of any compliant micro-positioning platform. This paper proposes a compliant micro-positioning platform (CMPP) with embedded strain gauges and a viscoelastic damper. The strain gauges, glued at the flexure hinges, measure the displacement of the CMPP and so serve as a displacement sensor. In the open-structured CMPP, the polydimethylsiloxane (PDMS) material which fills the cavity serves as a viscoelastic damper, increasing the stiffness and frequency of the CMPP. PDMS also has the function of harvesting undesired vibrations which affect the performance of the CMPP. The working principle of the developed gauge sensor is established. The effects of the geometric parameters on the strain and the stress distributions are investigated in order to assign the most suitable locations for the strain gauges on the elastic bodies. For purposes of comparison, the performance characteristics in cases without and with an embedded damper are investigated herein. An analytical dynamic model of the CMPP is then established through the Lagrange principle. The geometric parameters of the CMPP are optimized via the differential evolution algorithm. The sensitivity of the developed sensor is determined by the calibrations and the analytical model. It can be concluded that the platform with an embedded strain gauge can determine the displacement as a displacement sensor. The stiffness and the frequency of the platform are reinforced by the viscoelastic damper. The performances can be improved using the differential evolution algorithm. The results indicated that the proposed stage possesses the large range of motion of 860 μm and a high frequency of 345.2 Hz with an infinite fatigue-life of 5.67×10^7 cycles. It is believed that the platform has potential applications in micro-positioning manipulations, in situ microindentation and microscratch testing.

✉ Shyh-Chour Huang
shuang@cc.kuas.edu.tw

1 Division of Computational Mechatronics, Institute for Computational Science, Ton Duc Thang University, Ho Chi Minh City, Vietnam

2 Faculty of Electrical and Electronics Engineering, Ton Duc Thang University, Ho Chi Minh City, Vietnam

3 Department of Mechanical Engineering, National Kaohsiung University of Applied Sciences, 415 Chien-Kung Road, Kaohsiung 80778, Taiwan R.O.C.

1 Introduction

Micro-positioning platforms are now widely used to realize a highly precise location for accurate micro-positioning manipulations and assembly applications. Micro-positioning platforms increasingly require a high positioning accuracy and a large range of motion over several to a few hundreds of microns. The micro-positioning stages based on compliant mechanisms are widely utilized in different applications including X-ray lithography, nanoimprint lithography, micro-surgery scanning tunnel microscopy, micro surface metrology and characterization, atom force microscopy, and bio-medicine (Smith et al. 1987; Zubir and Shirinzadeh 2009; Miller et al. 1996; Tian et al. 2009; Mukhopadhyay et al. 2008). In the other words, compliant mechanisms can fulfill the requirements of micro-positioning platforms thanks to advantages such as monolithic manufacturing, free of friction, no wear, no lubrication, etc. (Dao and Huang 2015a, b). These micro-mechanical systems have been reported in great research efforts in recent years (Polit and Dong 2009; Choi et al. 2014; Guo et al. 2015) and some are

available on the market. Moreover, some have been utilized in the field of aerospace (Tsai et al. 2009) and in micro-/nanopositioning systems (Li and Xu 2011; Huang and Li 2010; Li et al. 2012; Tang and Li 2013).

In these reports, piezoelectric actuators were generally used to generate a load to the compliant micro-positioning stages, because of their high stiffness, good resolution, large force generation, fast response and low power consumption. In addition, to recognize the displacement of the compliant micro-positioning platforms, displacement sensors (Lin et al. 2015; Teo et al. 2014) or capacitive displacement sensors (Xi et al. 2016) have been combined with piezoelectric actuators.

For applications in microindentation and microscratching systems, piezoelectric actuators have been integrated with a capacitive displacement sensor to create a precision microindentation and microscratching system (Park et al. 2007). The piezoelectric actuator has also been combined with an optical fiber displacement sensor for a microindentation tester (Shimamoto and Tanaka 1997). In order to overcome the hysteresis and nonlinearity of the piezoelectric actuator, a real-time controlled closed-loop micro-positioning system integrated with a capacitive displacement sensor was reported (Shiou et al. 2010). These works are examples of the many different applications made possible by integrating the piezoelectric actuator and commercial displacement sensors or capacitive displacement sensors. Some compliant mechanisms have also been used in designing sensors and actuators on different scales (Wang and Hu 2005; Shakoor et al. 2011).

While both commercial displacement sensors and capacitive displacement sensors have a high accuracy, when these sensors are integrated with compliant micro-positioning platforms, a platform with a relatively large size is formed. In the cited works, special applications requiring limited dimensions were therefore restricted, for example, in situ micro mechanical tests inside a scanning electron microscope (SEM), or in a transmission electron microscope (TEM) investigating deformation and damage phenomena during the period of contact between an indenter and a sample (Warren et al. 2010; Rabe et al. 2004; Malyskaa et al. 2008; Huang et al. 2012). Micro indentation and scratch test significantly involves the precision detection technique, and thus compliant micro-positioning platforms are needed for such applications.

It is known that SEM and TEM have a small volume chamber, short working distance, electromagnetic sensing, vacuum environment and vibration sensing (Ghisleni et al. 2009). Thus, commercial displacement sensors or capacitive displacement sensors have limited use in these applications. Also, a complicated assembly of these sensors with a compliant micro-positioning platform results in measuring errors, as well as decreased stiffness and sensitivity of the compliant micro-positioning platforms. As a result, direct displacement measuring sensors with a more compact structure were required. A compliant micro-positioning platform is very sensitive to any internal or external vibrations, and a damper is needed to suppress these undesired vibrations. Polydimethylsiloxane material with viscoelastic properties has been effectively used as a vibration isolator (Huang et al. 2015). With this viscoelastic damper, the stiffness of a compliant micro-positioning platform can be reinforced and as a result its frequency will be also increased, thereby making the response of the platform faster. In the literature review, a compliant micro-positioning platform integrated with a strain gauge and a viscoelastic damper has yet to be proposed.

This study is aimed to design and analyze of a new compliant micro-positioning platform. The developed platform is embedded with strain gauges and a viscoelastic damper. The platform with embedded strain gauges is considered as a developed gauge sensor that comprises a frame of flexure hinges, strain gauges and a piezoelectric actuator. The strain gauges are glued to the surfaces of the flexure hinges, while the piezoelectric actuator is used to generate a load onto the movable object of the platform. The output displacement of the platform is directly measured by the developed sensor. The platform has an open cavity which was filled with the polydimethylsiloxane material. This material serves as a viscoelastic damper to eliminate undesired vibrations and reinforce the stiffness of the platform, thereby making the response of the platform faster. Both the working principle and mathematical model of the developed gauge sensor are established, and prototypes are manufactured by means of wire electrical discharge machining. The effects of the geometric parameters on the strain and stress distributions are then investigated to assign suitable locations for the strain gauges on the elastic bodies. Two case studies without and with an embedded damper are compared to determine the performance characteristics, including strain, displacement, first natural frequency and stiffness. An analytical dynamic model of the platform is then established using the Lagrange principle. The geometric parameters are optimized via the differential evolution algorithm to maximize the frequency and range of motion. From the optimal dimensions, the sensitivity of the developed sensor is determined by the calibrations and the analytical model.

2 Compliant micro-positioning platform with embedded strain gauges and viscoelastic damper

2.1 Structural design

In this study, a compliant micro-positioning platform (CMPP) was incorporated with strain gauges and a viscoelastic damper to form a displacement sensor, as depicted in Fig. 1. The platform comprised two groups of flexure

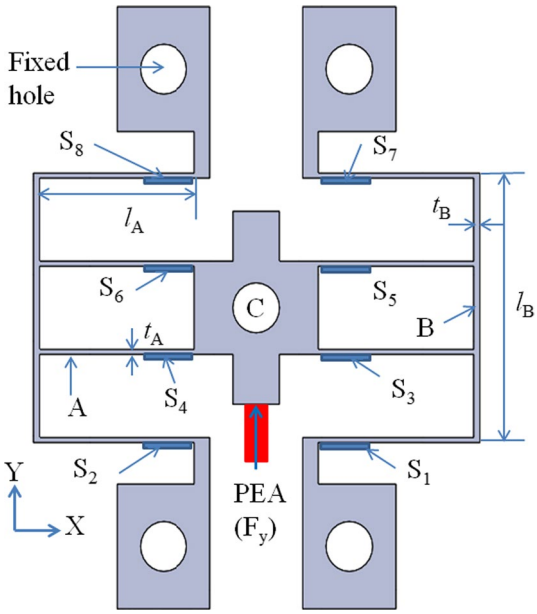

Fig. 1 A compliant micro-positioning platform (CMPP) with embedded strain gauges

hinges, a movable object and eight strain gauges. The platform was designed as a symmetrical I-shaped structure, where a large displacement only along the y-axis was desired. The flexure hinges were divided into types A and B. Each flexure hinge was considered as an elastic body, and each elastic body was considered as a substrate, with each sensor gauge integrated on the surface of the substrate. The fact that that, the A group must be constructed with flexure hinges to achieve a translational motion along the y-axis. Noted that the B group could be also designed with traditional rigid links but such the rigid links would result in a decrease in the displacement of the platform. Hence, the B group should be created via using flexure hinges. And so-called elastic bodies would be support in increasing the displacement of the platform. The piezoelectric actuator (PEA) generated a load F_y on the platform. Material Al 7075 was selected for the platform because of its high yield strength of 435 MPa, Young's modulus of $E = 72{,}000$ MPa, light density of 2770 kg/m^3 and Poisson's ratio of 0.33.

The A group of flexure hinges included eight elastic bodies of the same length, l_A, width, w_A, and thickness, t_A, organized in the horizontal direction. The function of group A was to generate the translational motion for the movable object C along the y-axis resulting from the applied load F_y. The B group of flexure hinges consisted of two elastic bodies of the same the length, l_B, width, w_B, and thickness, t_B, organized in the vertical direction; the function of this group was to support a larger displacement for the movable object C along the y-axis.

The eight strain gauges: S_1, S_2, S_3, S_4, S_5, S_6, S_7 and S_8, were glued using an appropriate adhesive to the surfaces of the A group of flexure hinges at suitable positions. The deflection of these flexure hinges was detected by the strain gauges. S_1, S_3, S_5 and S_7 were organized on the surfaces on the right side of the CMPP, while S_2, S_4, S_6 and S_8 were located on the surfaces at the left side of the CMPP. The platform was located at the fixed holes.

The platform's open cavities were filled with viscoelastic material. The polydimethylsiloxane (PDMS), a viscoelastic silicon rubber material, served as a viscoelastic damper for the platform. The prototypes without a damper and with an embedded damper are shown in Fig. 2a, b, respectively. The function of the PDMS was to increase the

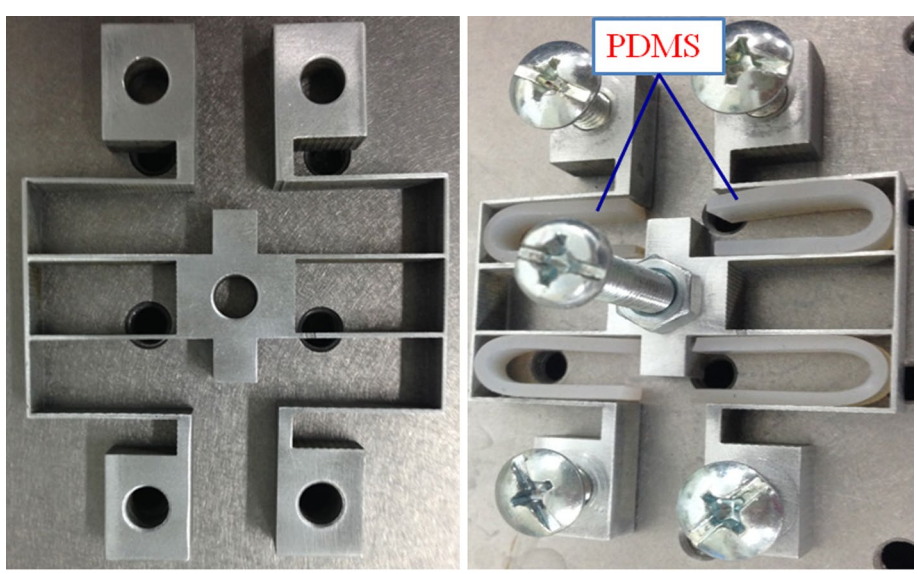

(a) (b)

Fig. 2 Prototypes of CMPP in: **a** without embedded damper and **b** with embedded damper

stiffness of the platform on both the x-and y-axes, particularly along the x-axis. The speed of the compliant micro-positioning platform increased as a result of the frequency of the platform also increasing.

As compared with previous platforms integrated with laser displacement sensors or capacitance sensors, the developed compliant micro-positioning platform was more compact because of the embedded strain gauges. Also, the proposed platform was able to eliminate undesired vibrations from inside or outside disturbances because of the embedded viscoelastic damper, and the stiffness of the platform was also increased due to the embedded viscoelastic damper.

In this study, a viscoelastic PDMS damper was integrated with the compliant micro-positioning platform to suppress undesired vibrations to improve its efficiency, see Ref. (Huang et al. 2015); to reinforce the stiffness of the developed platform; and to enhance the frequency of the platform because a higher frequency means a faster platform speed.

2.2 Working principle of developed strain gauge sensor

The displacement sensor as built, based on the strain gauges and the flexure hinges, is shown in Fig. 1. When an input voltage signal V_{ex} is applied to the piezoelectric actuator, a generated load is exerted on the movable object, C, and the flexure hinges are deflected. The output displacement is recorded. At the same time, the displacement of the flexure hinges also results in deformation of the strain gauges, which changes their electrical resistance, R.

The strain-gauge sensor, designed to measure the output displacement along the y-axis of the platform, is compact. A suitable position must be found where the strain has a maximum value in order to improve the sensitivity of the sensor. The best positions for the sensor location can be determined by finite element analysis (FEA) simulations. The resistance change is converted into a change in the corresponding voltage through a half-Wheatstone bridge circuit, as shown in Fig. 3.

The working principle of the developed displacement gauge sensor in this study is illustrated in Fig. 1. The next analysis establishes the mathematical models for the developed sensor. The elastic theory of flexure hinges and the theory of the half-Wheatstone bridge circuit are combined to develop the mathematical equations of the proposed displacement gauge sensor. As seen in Fig. 3, if the platform is under tension, the resistance R will increase by a value of ΔR. Conversely, in the case of compression, the resistance R will decrease by a value of ΔR.

The gauge factor of the strain sensor is defined as the ratio of fractional change in the electrical resistance to the fractional change in length:

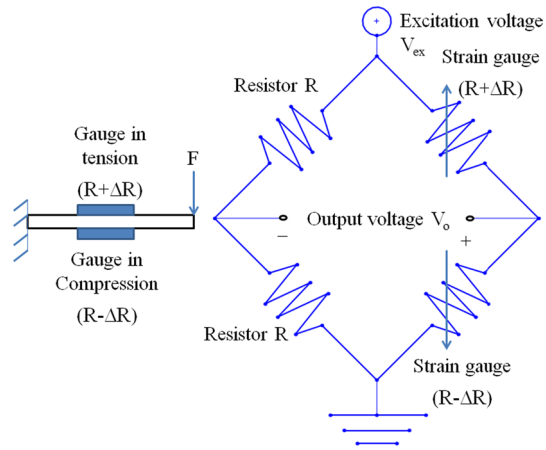

Fig. 3 Half-Wheatstone bridge circuit of the strain gauge

$$G = \frac{\Delta R}{R \times \varepsilon} \tag{1}$$

where G is the gauge factor of the strain gauge; ΔR is the change in value of the gauge resistance; R is the nominal value of the gauge strain as an undeformed strain gauge; and ε is the strain.

The strain is related to the resulting stress by the following equation:

$$\sigma = E \times \varepsilon \tag{2}$$

where σ is the resulting stress and E is the Young's modulus of the material Al 7075.

The output voltage of the circuit is approximated by the following equation:

$$V_o = \frac{G\varepsilon}{2} \times V_{ex} = \frac{\Delta R}{2R} \times V_{ex} \tag{3}$$

where V_o is the output of the circuit and V_{ex} is the excitation voltage of the circuit.

Substituting Eqs. (1) and (2) into (3), the output voltage of the circuit is approximated by the following equation:

$$V_o = \frac{G\sigma}{2E} \times V_{ex} \tag{4}$$

Equation (4) signifies that the output voltage is proportional to the resulting stress of the flexure hinges.

One flexure hinge, A, is selected in order to analyze the sensitivity of the displacement sensor gauge. Each flexure hinge has a linear stiffness calculated as follows:

$$K_A = \frac{Ewt_A^3}{l_A^3} \tag{5}$$

where K is the stiffness of the flexure hinge.

The force F_y is related to the displacement δ of the flexure hinge by the relation:

$$F_y = K_A \times \delta \tag{6}$$

The force F_y is related to the resulting stress of the flexure hinge by the relation:

$$\sigma = \frac{6F_y l_A}{wt_A^2} \tag{7}$$

Substituting Eqs. (5), (6) and (7) into (4) gives as follows:

$$V_o = \frac{3V_{ex}Gt_A}{l_A^2} \times \delta \tag{8}$$

Equation (8) is equivalent to:

$$V_o = S \times \delta \tag{9}$$

where S is the sensitivity of the strain gauge is calculated by the following equation:

$$S = \frac{3V_{ex}Gt_A}{l_A^2} \tag{10}$$

Combining Eqs. (2) and (7), the strain is related to the geometric parameters of the flexure hinge as:

$$\varepsilon = \frac{6F_y l_A}{Ewt_A^2} \tag{11}$$

In practice, by determining the output displacement of the platform and the output voltage, the sensitivity S of the strain gauge can be determined via calibrations; these show the linear relation of the output voltage of the strain gauge with the displacement of the platform. In addition, the sensitivity is related to the excitation voltage, the gauge factor and the geometric parameters of the platform. As seen in Eq. (11), the geometric parameters of the flexure hinge have a significant impact on the strain. After the working principle of the strain gauge sensor is determined, the suitable positions of the strain gauges integrated on the substrate are determined by the FEA simulations.

2.3 Location assignment of embedded strain gauge

A simplified model of flexure hinge of the A group is depicted in Fig. 4. The flexure hinge serves as the substrate on which the strain gauges are located. Because the strain gauge is very lightweight, the strain gauge is not installed on the surface of the substrate for the FEA simulations in ANSYS 2015.

The model consists of two ends, D and E. On the left side, end D is a fixed position. On the right side, end E is the freedom location for applying a movable load. The freedom location applies an input displacement of 1 mm along the negative y-direction. The material Al 7075 selected for

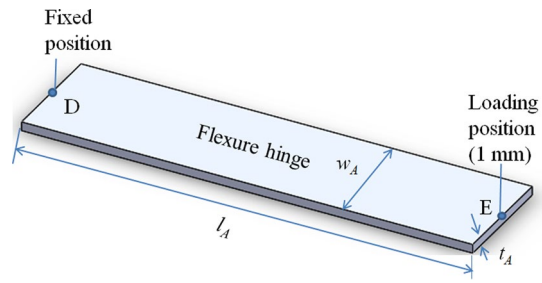

Fig. 4 Simplified model of flexure hinge with load of 1 mm

the model. The geometric design parameters of the flexure hinge mainly affect the strain and stress. The parameters set for the simulations were as follows: $l_A = 20$, 24, 27 and 30 mm; $w_A = 5$, 6, 7 and 8 mm; and $t_A = 0.4$, 0.5, 0.6 and 0.7 mm.

Through the simulations, the suitable positions for the sensor gauge locations are found. As shown in Fig. 5, the strain distribution along the red straight line DE of the flexure hinge is numbered from 1 to 20, which indicates that the strain distribution on the left side of the flexure hinge is symmetric to that on the right. The symmetric point is at the middle point, number 10 (area in blue), through the horizontal center line. Hence, only the strain of the numbers in the range from 10 to 20 is investigated.

In practice, the strain gauge is attached at the top and bottom surfaces of the flexure hinge to measure the strain in the tension and compression directions, respectively. The strain in tension at the top surface is equal to the strain at the lower surface in the compression direction. On the top surface, the strain has a positive value; while at the lower surface, the strain has a negative value.

As seen in Fig. 6, the strain is changed as a result of a change in the length of the flexure hinge. The maximum strain was at the left or right side of the flexure hinge. The lowest strain was at the middle point, number 10. It can be seen that the maximum strain corresponded to the minimum length of the flexure hinge ($l = 20$ mm), followed by $l = 24$ mm, $l = 27$ mm and the lowest strain with respect to $l = 30$ mm.

It could be concluded that the strain distribution was mainly affected by the length of the flexure hinge. The strain gauge should be attached at the left end area D or around the right end area E where a load is applied.

The width of the flexure hinge, however, had almost no effect on the strain, as evident in Fig. 7. A change in the width of the flexure hinge ($w = 5$ mm, $w = 6$ mm, $w = 7$ mm, $w = 8$ mm) did not affect the strain, an indication that the strain was not sensitive to changes in the width of the flexure hinge.

As shown in Fig. 8, the strain did vary with a change in the thickness of the flexure hinge, with the strain increasing as the thickness increased. The maximum strain was at the

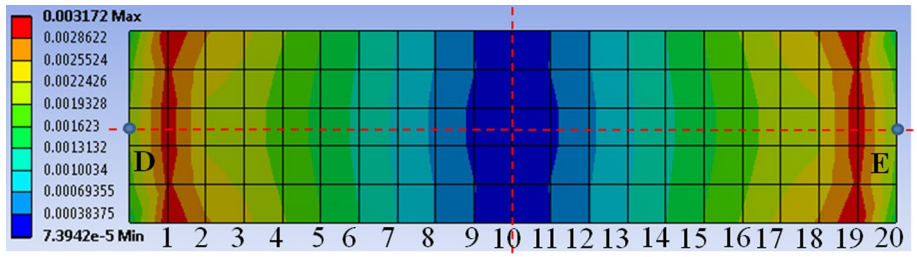

Fig. 5 Strain distribution along the line DE of the flexure hinge

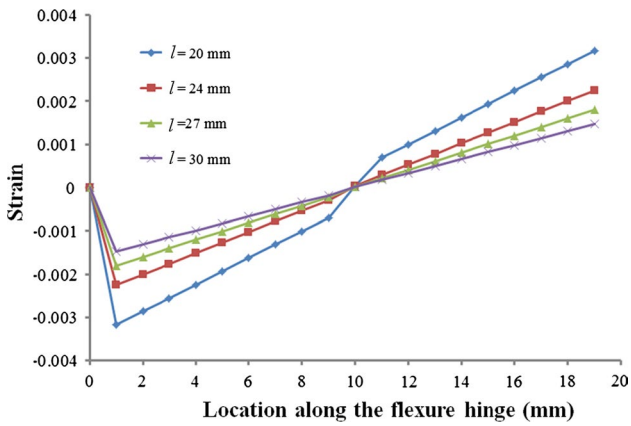

Fig. 6 Strain distribution with different lengths of flexure hinge

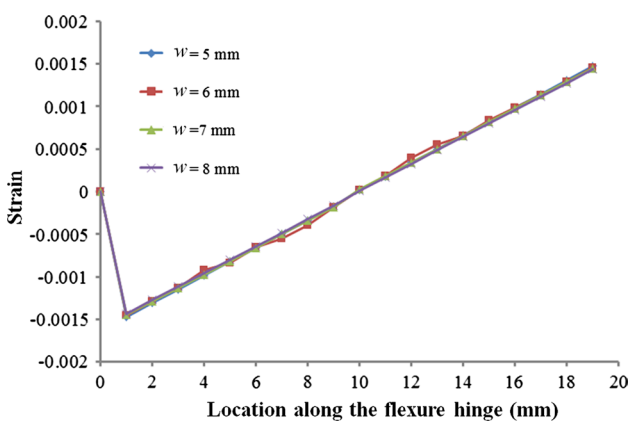

Fig. 7 Strain distribution with different widths of flexure hinge

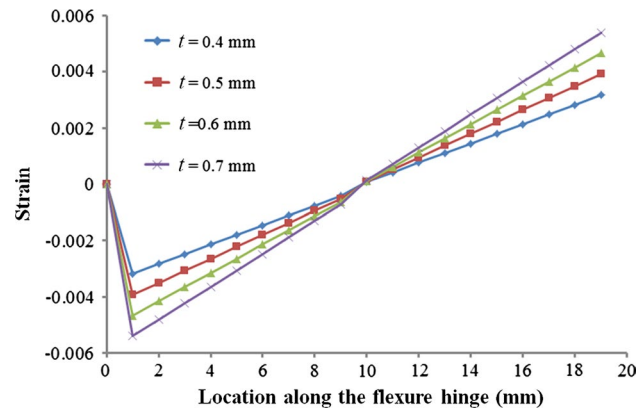

Fig. 8 Strain distribution with different thicknesses of flexure hinge

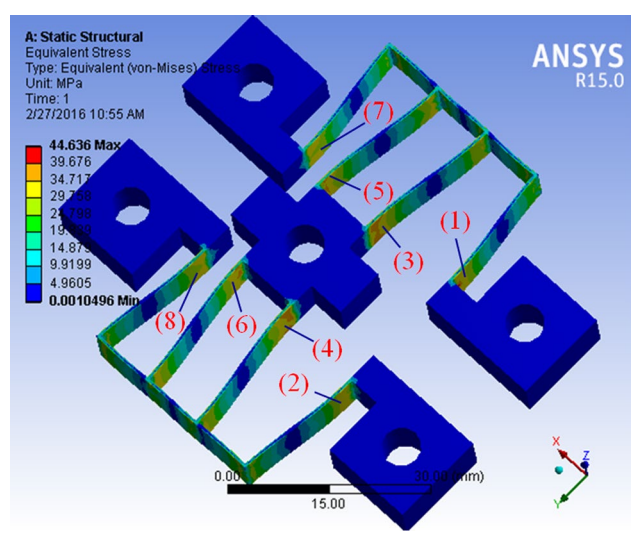

Fig. 9 Stress distribution of flexure hinge

left or right side of the flexure hinge, and the lowest strain was at the middle point, number 10. The maximum strain corresponded to the maximum thickness of the flexure hinge ($t = 0.7$ mm), followed by $t = 0.6$ mm, $t = 0.5$ mm and the lowest strain with respect to $t = 0.4$ mm. It could be concluded that the strain was very sensitive to any change in the thickness of the flexure hinge.

To sum up, the length and thickness of the flexure hinge should be selected carefully, and the strain gauges should be attached at suitable positions to obtain the necessary measurement accuracy.

For a load of 1 mm along the y-axis, Fig. 9 demonstrates the stress distribution of the platform, which has eight positions numbered (1), (3), (5) and (7) on the right

side and (2), (4), (6) and (8) on the left side. These eight positions predict the maximum equivalent stress near the area of applied load. The strain–stress analysis showed that the strain gauges should be located on the top surface of the flexure hinges in an area near the applied load. Positions (1), (3), (5) and (7) were selected to integrate with the embedded strain gauges.

3 Experiments

3.1 Strain–stress analysis

As per the above analysis, suitable positions were found for the strain gauges to be embedded in the platform. The strain is related to the stress through Hooke's law. The stress is also related to the fatigue life by Eq. (12). For any compliant joints, a major concern is fatigue induced by completely reversed stress because a flexible component frequently repeats its motion. This relation is briefly described in (Shigley and Mischke 1989):

$$N = \left(\frac{\sigma}{a}\right)^{1/b} \tag{12}$$

$$a = \frac{(fS_{ut})^2}{S_e} \tag{13}$$

$$b = -\frac{1}{3}\log\left(\frac{fS_{ut}}{S_e}\right) \tag{14}$$

where N is the number of cycles-to-failure; S_{ut} is the ultimate strength; S_e is the endurance limit; and f is a constant.

The strain on the CMPP is one of the most important concerns, so the maximum stress needs to be determined. In this study, four different positions on the CMPP, numbered (1), (3), (5) and (7), were used to test the strain (see Figs. 1, 5). As the CMPP is a symmetric structure, only these positions were evaluated.

The PDMS damper was integrated in the compliant micro-positioning platform to reinforce the stiffness of the developed platform; to improve the frequency of the platform because a higher frequency means a faster platform speed; and to suppress undesired vibrations. In addition, the viscoelastic properties of the damper can affect the strain of the proposed platform. Hence, many simulations and experiments were carried out to investigate these effects.

Figure 10a, b show the strain measurements of the platform without a damper and with an embedded damper, respectively. The calibration instruments included a force gauge (Lutron, tension and compression, maximum 196 N, DC 9 V adapter, model: NF-9500, Taiwan) to adjust the applied force; a sensor gauge (KFG 5-120-C1-11L1M2R, KYOWA, Japan) with a gauge factor of 2.07, resistance of 120.4 Ω and excitation voltage of 2.5 V; a CPU (computer processing unit, ASUS); DAQ (data acquisition, National Instruments, Japan); and a screen (ASUS). The prototype was mounted onto a base fixed to the vibration isolation system table in order to suppress any vibrations. Four sensor gauges were glued at the four positions to measure the actual strain. Each position was measured separately. The experiments were repeated five times to obtain the average value. The force gauge was adjusted to gradually reach a desired value. Data from the sensor gauge were transferred to the DAQ instrument, which generated data to the CPU.

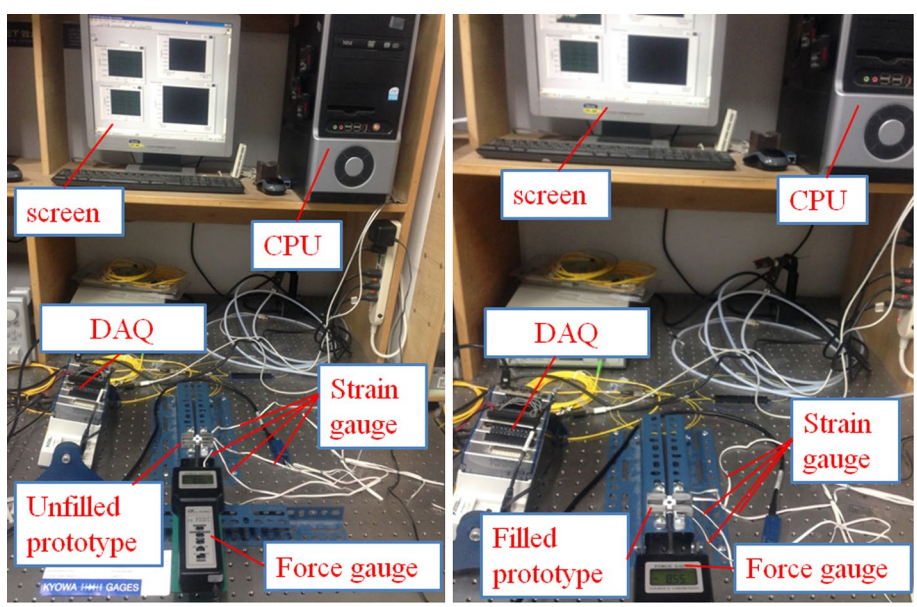

Fig. 10 Experimental strain for CMPP: **a** without damper and **b** with embedded damper

LABVIEW® software was set up in the CPU so that the strain wave and value of the strain were displayed on the screen. The strain value after each experimental measure was recorded.

The different values of force gauge such as 4, 6, 8, and 10 N were exerted to the platform, individually. When the platform moved, the flexure hinges were deflected and the strain data was recorded. As aforementioned, there were only positions including (1), (3), (5) and (7) that their strain and corresponding stress were assessed. And then a FEA analysis for case without the damper was carried out for these positions.

For position (1), the physical strain values with the embedded damper were about 13.2 % smaller than those and FEA values without the damper, as seen in Fig. 11a. The experimental results were in a good agreement with the FEA ones with an error of 1.04 %. Similarly, many experimentations and FEA analyses were performed for the positions (3), (5) and (7). For position (3), the physical strain values with the damper were approximately 14.49 % lower than those and FEA values without the damper, as seen in Fig. 11b. The experimental results were in a good agreement with the FEA ones with an error of 4.98 %. For position (5), the physical strain values with the damper were about 6.4 % lower than those and FEA values without the damper, as seen in Fig. 11c. The experimental results were in a good agreement with the FEA ones. For position (7), the physical strain values with the damper were about 6.9 % smaller than those and FEA values without the damper, as seen in Fig. 11d. The FEA results were close to the experimental results. The strain values in the case of without the damper were higher than those of with the embedded damper. The reason was only that the stiffness of the platform was reinforced the damper PDMS. This is also a highlight of this study in combining the compliant micro-positioning platform with the viscoelastic damper. Besides, the maximum strain was found at the position (7). As the maximum stress at this position affected the fatigue life of the platform, it required careful consideration to guarantee the safety operation. The experimental results were a little bit difference with the simulation results due to manufacturing and assemble errors.

According to Hook's law, using Eq. (2), the stress for the platform was calculated by determining the strain in advance. Figure 12a–d illustrate the stress results for the four positions, respectively. All four positions, (1), (3), (5) and (7), in the physical experiments showed that stress in case without the damper is about 13.2 % higher than that of case with the embedded damper. In the simulations, the FEA stress without a damper was approximately 14.4 % greater than that of case with the embedded damper. The maximum stress was at the position (7). This position must be considered carefully because the maximum stress has the strongest influence on the fatigue life of the platform, according to Eq. (12). The experimental results were in a good agreement with the simulation results. Aforementioned, the damper PDMS

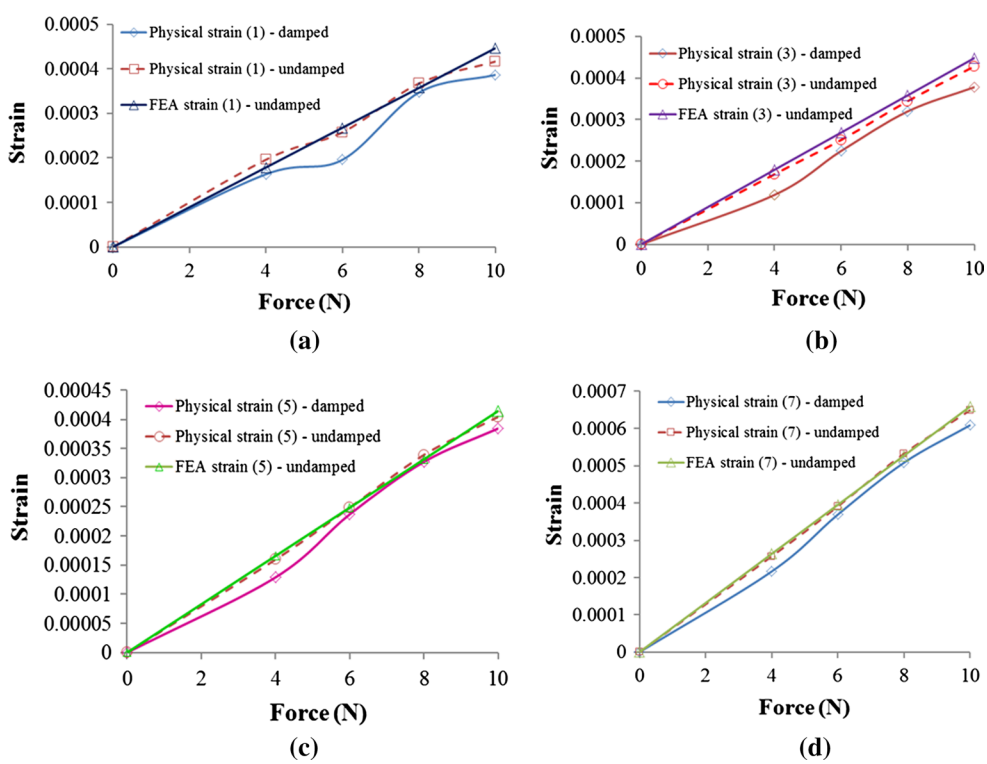

Fig. 11 Strain for four different positions (1, 3, 5, 7) of the CMPP

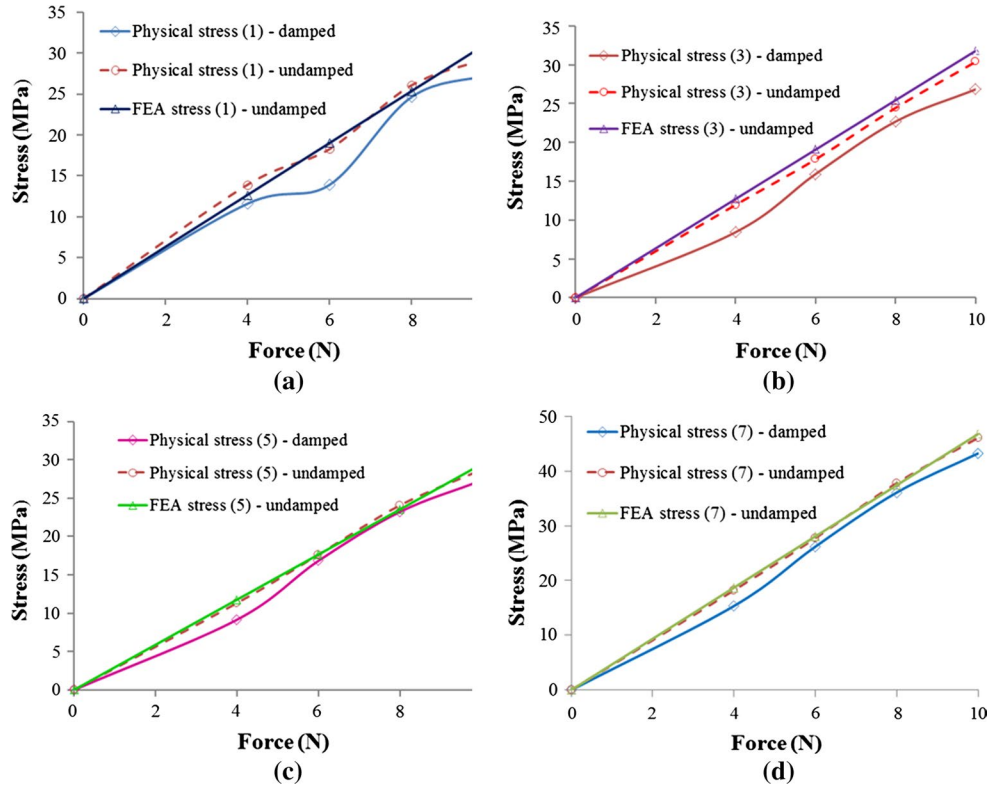

Fig. 12 Stress for four different positions (1, 3, 5, 7) of the CMPP

increased the stiffness of the platform and thus the strain was decreased. As known, the stiffness is conflicted with the strain or stress. It could be concluded that the damper PDMS also decreases the stress. Hence, the platform can operate with a long fatigue life cycle. The PDMS is capable to reinforce the stiffness of the platform.

3.2 Stiffness analysis

The second purpose of the viscoelastic damper was to support the stiffness of the developed platform. In this approach, the stiffness of the elastic body resulted in a change in the dynamic response of the platform.

Many simulations and experiments were conducted to investigate this characteristic of the PDMS damper. Figure 13a, b depict the experimental setup of the range of motion of the CMPP along the y-axis without the damper and with the filled damper, respectively. A force gauge was used to make the necessary adjustments to achieve the different values, including 0.2, 0.4, 0.6, 0.8 and 1 N. An end of CMPP was fixed. A laser displacement sensor (Keyence, Japan) was used to measure the displacement of the CMPP, and a connector was utilized to transfer the signal to a digital display. Each experiment was repeated four times and the average result was calculated.

As seen in Table 1, the average stiffness in the case without the PDMS damper was calculated about 0.012 N/μm, while the average stiffness in the case with the embedded PDMS damper was computed approximately 0.013 N/μm. Besides, the results showed that the displacements in the y-axis of the platform in case with the embedded damper are much smaller than those of case without the damper, i.e., a decrease in displacement about 4.96, 5.2, 2.4, 1, and 3.6 % with respect to 0.2, 0.4, 0.6, 0.8 and 1 N, respectively. It could be concluded that the stiffness of the developed micro-positioning platform increased when the open cavities were embedded with the viscoelastic PDMS damper. The results provided helpful information regarding the design process of compliant micro-positioning stages, particularly that the stiffness can be reinforced by the extra damper. The simulation results were close to the experimental results.

To prove that the stiffness of the platform actually increased, various simulations and experiments with a load along the x-axis were performed. For the experimentations, the CMPP was affixed to the table. The force gauge was employed to determine the different loads of 2, 4, 6, 8 and 10 N on the x-axis. According to the design process, the displacement of the platform along the x-direction might be less than that along the y-direction, and the greater loads were thus applied to the platform along the x-axis. The digital indicator was used to record the range of motion of the CMPP. The experimental setups for the CMPP without the damper and with the filled damper are shown in Fig. 14a, b, respectively.

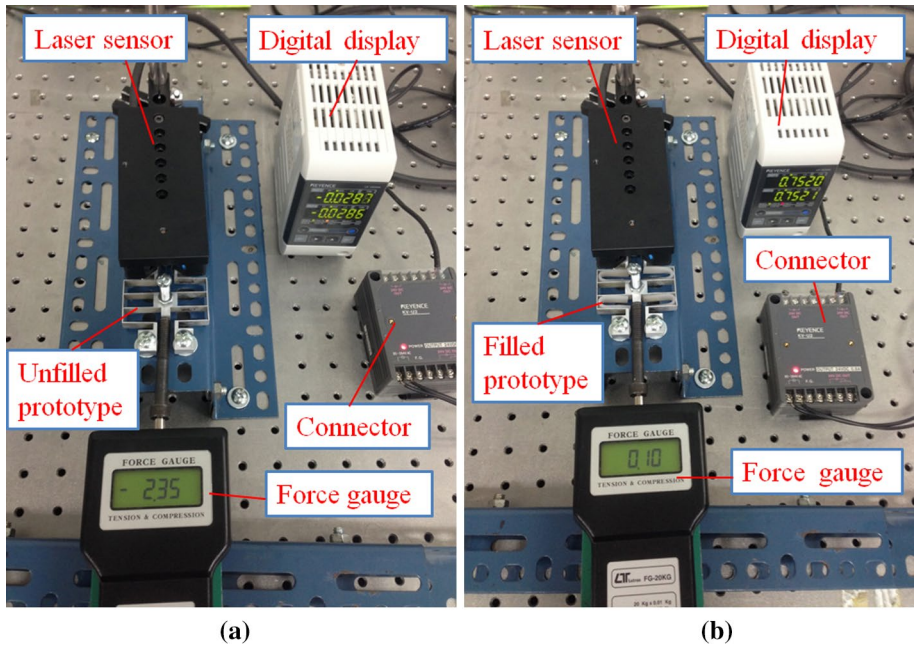

Fig. 13 Displacement along y-direction of the CMPP: **a** without the damper and **b** with the embedded damper

Table 1 Displacement along y-direction (units: μm)

Displacement (μm) in cases	Applied force (N)				
	0.2 N (μm)	0.4 N (μm)	0.6 N (μm)	0.8 N (μm)	1 N (μm)
Experiment without damper	16.1	32.4	48.3	65.4	82.8
Experiment with damper	15.3	30.7	47.1	64.7	79.8
FEA without damper	16.6	33.3	49.9	66.6	83.2
FEA with damper	15.8	29.1	47.8	65.0	81.3

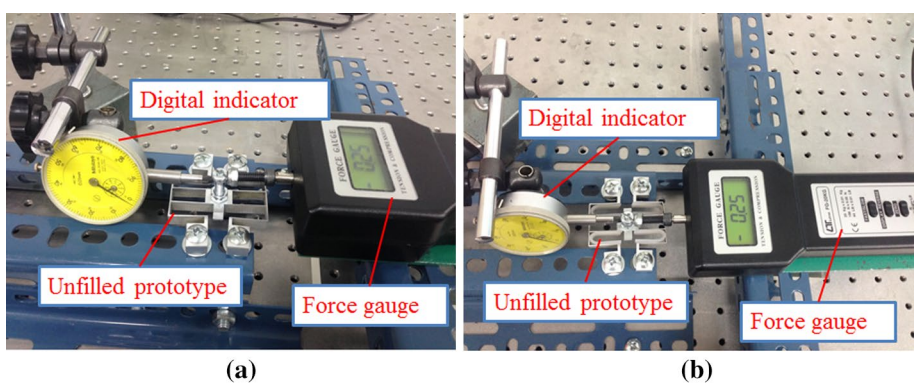

Fig. 14 Stiffness measurement along the x-direction of the CMPP: **a** without the damper and **b** with the embedded damper

Table 2 Displacement along the x-direction (units: μm)

Displacement (μm) in cases	Applied force (N)				
	2 N (μm)	4 N (μm)	6 N (μm)	8 N (μm)	10 N (μm)
Experiment without damper	21.4	45.3	68.1	90.6	104.8
Experiment with damper	21.2	45.0	67.7	90.2	104.5
FEA without damper	23.1	46.2	69.4	92.5	115.6
FEA with damper	21.0	45.1	68.0	90.5	104.7

For the applied loads in the x-direction, the average stiffness without the PDMS damper was determined about 0.0908 N/μm, while the average stiffness with the embedded PDMS damper was calculated about 0.0916 N/μm, as shown in Table 2. Similarly, the results indicated that the displacements of the platform in the x-axis of case with the embedded PDMS are a little bit lower than those of case without the PDMS, i.e., a decreased displacement about 0.9, 0.6, 0.5, 0.4, and 0.2 % corresponding to the applied forces of 2, 4, 6, 8 and 10 N, respectively. The experimental results were in a good agreement with the FEA results. It proved that the stiffness of the platform increased when the open cavities were embedded with the viscoelastic PDMS damper.

3.3 Frequency response

The dynamic response of the proposed platform was evaluated as the third purpose of the viscoelastic damper that is to improve the frequency of the platform.

The measurements of the first natural frequency within the range of 100 Hz to 500 kHz were performed in order to evaluate the dynamic characteristics of the mechanism without pre-stress, i.e., no piezoelectric actuator (PEA). A modal hammer (Model 9722A2000-SN 2116555, Kistler) was used to apply the excitation to the mechanism, and the frequency response was measured by using an accelerator (Model 4744892, Kistler). The accelerator was attached the place where is opposite to the location of the excitation of the modal hammer. A modal analyzer (Model NI USB 9162, National Instruments) was utilized for the data acquisition and analysis. A force sensor attached to the end of the hammer was used to measure the applied force from the hammer. CUTPRO software was installed in a computer to analyze the data. The experiments were repeated five times. The experiment without the PEA and without the damper is presented in Fig. 15a; the frequency of 125 Hz is recorded in Table 3. The experiment without the PEA and with the damper is given in Fig. 15b; the frequency of 139 Hz is recorded in Table 3. The results revealed that the frequency in the case without the PDMS damper was lower than in the case with the filled PDMS damper because the use of the PDMS increased the stiffness of the platform.

A high-speed bipolar amplifier (Model HAS 4011, NF Corporation) was utilized to drive the PEA (Model 150/5/40 VS10, Piezomechanik GmbH). Retro-reflective tape (Ono Sokki Company) was attached at the middle of the movable object. A preload was applied on the PEA. A laser vibrometer sensor (Model LV-170, Ono Sokki Company) with a high nanoscale resolution was used to measure the displacement. A frequency response analyzer (Model FRA 5097, NF Corporation) was used, and frequency response analyzer display software was installed in the computer. Using the FRA display software, the data were displayed as diagrams. Overall experiments were repeated five times to obtain the average of the measured values. The experiment with the PEA but without the damper is shown in Fig. 16a;

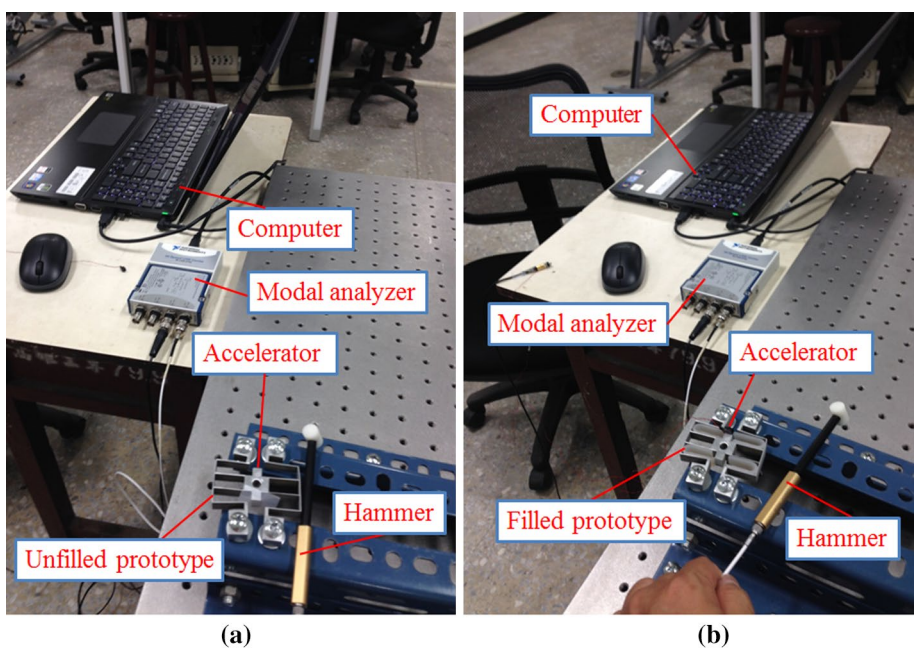

Fig. 15 Frequency of the CMPP via hammer: **a** without damper and **b** with embedded damper

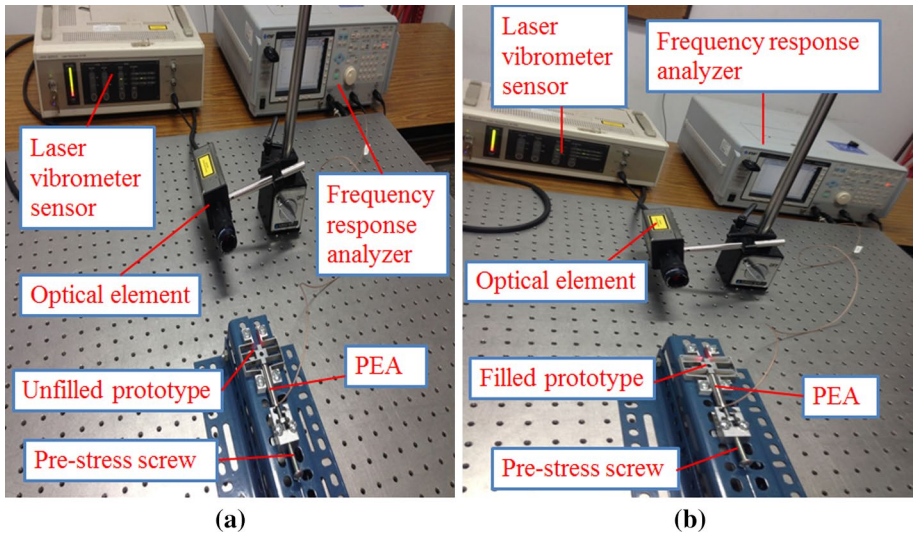

Fig. 16 Frequency of the CMPP driven via PEA: **a** without damper and **b** with embedded damper

Table 3 First natural frequency (units: Hz)

Not PEA and not damper	Not PEA and embedded damper	Driven PEA and not damper	Driven PEA and embedded damper
125 Hz	139 Hz	3700 Hz	3710 Hz

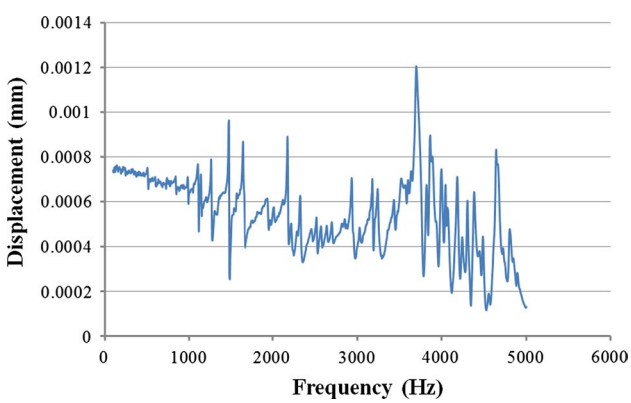

Fig. 17 Frequency versus displacement in case of the PEA without the damper (3700 Hz)

the frequency of 3700 Hz is recorded in Table 3 and Fig. 17. The experiment with the PEA and with the damper is presented in Fig. 16b; the frequency of 3710 Hz is recorded in Table 3 and Fig. 18. The results indicated that the frequency in the case without the PDMS was lower than in the case with the filled PDMS damper as the use of the PDMS resulted in an increase in the stiffness of the platform.

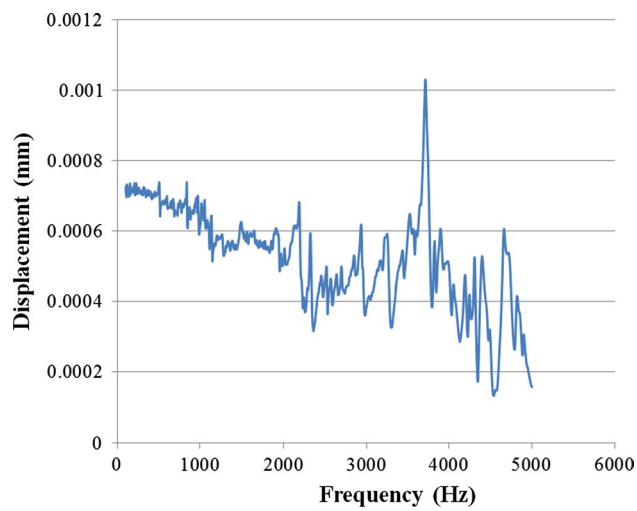

Fig. 18 Frequency versus displacement in case of the PEA with the embedded damper (3710 Hz)

To sum up, as shown in Table 3, the frequency increased when the PDMS damper was embedded in the open cavities; it could be concluded that the PDMS resulted in increased stiffness. In reality, when a compliant positioning platform becomes stiffer, the frequency is also increased; hence, the speed of the proposed platform was enhanced as well, and the platform operated at a high frequency.

4 Optimization of micro-compliant positioning platform

The analysis determined that the proposed platform was very sensitive to the length and the thickness of the flexure hinges. Hence, the optimization problem was very necessary in order to optimize those parameters and improve the performances of the platform. In general, before implementation of an optimization problem, a mathematical model is established.

The platform was designed as a fixed-guided flexible mechanism; thus, its dynamic model was based on the pseudo-rigid-body model (PRBM) as proposed by Ref. (Howell 2001).

The masses of part A, part B, and part C are calculated as follows:

$$M_A = N_A \times \rho \times (l_A \times w_A \times t_A) \tag{15}$$

$$M_B = N_B \times \rho \times (l_B \times w_B \times t_B) \tag{16}$$

$$M_c = \rho \times (22.5 \times 15.97 \times 8) - \rho \times 4 \times (6 \times 4 \times 8) - \rho \times \pi \times 3^2 \times 8 \tag{17}$$

where M_A, M_B and M_C are the corresponding masses of part A, part B and C, respectively; ρ is the density of the Al 7075 material; N_A is the number of flexure hinges (8 elastic bodies) belonging to part A; and N_B is the number of leaf springs B (2 elastic bodies).

The total mass M of the platform yields:

$$M = 8 \times \rho \times (l_A \times w_A \times t_A) + 2 \times \rho \times (l_B \times w_B \times t_B) + \rho \times (22.5 \times 15.97 \times 8 - 4 \times 6 \times 4 \times 8) \tag{18}$$

The natural frequency can be obtained from the dynamic equation of Lagrange's principle. Assuming that the proposed platform is moving along the y-axis, part B is assumed to be ideal rigid links. The kinetic energy T of the stage is calculated as:

$$T = \frac{1}{2} M \dot{y}^2 \tag{19}$$

The potential energy V resulting from the torsional springs of the flexure hinges according to the PRBM is:

$$V = 16 \times \frac{1}{2} K_{ds} \theta_z^2 \tag{20}$$

The dynamic stiffness K_{ds} of each torsional spring is determined as:

$$K_{ds} = 2\gamma k_\Theta \frac{EI_A}{l_A} \tag{21}$$

where $\gamma = 0.85$; $k_\Theta = 2.669$ (Howell 2001); E is the Young's modulus of material Al 7075; I_A is the moment of inertia $I_A = w_A t_A^3/12$; and $\theta_z = y/2l_A$ (Howell 2001) is the rotational angle along the z-axis.

Hence, Eq. (20) becomes:

$$V = 16 \times \frac{1}{2} K_{ds} \left(\frac{y}{2l_A} \right)^2 \tag{22}$$

To allow a free motion, the free motion dynamic equation of the platform is determined according to Lagrange's equation as:

$$\frac{d}{d_t}\left(\frac{\partial T}{\partial \dot{y}} \right) - \frac{\partial T}{\partial y} + \frac{\partial V}{\partial y} = 0 \tag{23}$$

Equation (23) is equivalent to:

$$M\ddot{y} + \frac{4K_{ds}}{l_A^2} y = 0 \tag{24}$$

And Eq. (24) is similar to:

$$M\ddot{y} + Ky = 0 \tag{25}$$

With the stiffness of the platform as:

$$K = \frac{4K_{ds}}{l_A^2} \tag{26}$$

The natural frequency of the platform f_{CMPP} is determined as:

$$f_{CMPP} = \frac{1}{2\pi} \sqrt{\frac{4K_{ds}}{Ml_A^2}} \tag{27}$$

As a result, Eq. (27) becomes:

$$f_{CMPP} = \frac{1}{2\pi}\sqrt{\frac{4K_{ds}}{(N_A \times \rho \times (l_A \times w_A \times t_A) + N_B \times \rho \times (l_B \times w_B \times t_B) + \rho \times (22.5 \times 15.97 \times 8 - 4 \times 6 \times 4 \times 8))l_A^2}}$$
$$= \frac{1}{2\pi}\sqrt{\frac{4K_{ds}}{(N_A \times (l_A \times w_A \times t_A) + N_B \times (l_B \times w_B \times t_B) + (22.5 \times 15.97 \times 8 - 4 \times 6 \times 4 \times 8))\rho l_A^2}} \quad (28)$$

The displacement of the platform δ_{CMPP} is determined according to Howell (2001) as:

$$\delta_{CMPP} = 2\sigma\max l_A^2 \Big/ 3Et_A \quad (29)$$

where σ_{max} is the maximum stress of the platform that is determined according to Howell (2001) as

$$\sigma\max = \frac{6F\max l_A}{w_A t_A^2} \quad (30)$$

The objective functions of the platform are briefly described as follows: the platform needs a large range of motion δ_{CMPP} over 800 µm along the y-axis for many applications and a high-frequency f_{CMPP} to increase the responding speed of the platform. The multi-objective optimization problem is stated as follows.

$$\text{Maximize } \delta_{CMPP} \quad (31)$$

$$\text{Maximize } f_{CMPP} \quad (32)$$

Subject to constraints:

$$\sigma\max \le \frac{\sigma_y}{n} \quad (33)$$

$$\begin{cases} 15\,\text{mm} \le l_A \le 25\,\text{mm} \\ 0.5\,\text{mm} \le t_A \le 1.5\,\text{mm} \\ 30\,\text{mm} \le l_B \le 48\,\text{mm} \\ 0.5\,\text{mm} \le t_B \le 1.5\,\text{mm} \end{cases} \quad (34)$$

where f_{CMPP} is the cost function of the natural frequency σ_y is the yield strength of material Al 7075 (435 MPa); and n is the safety factor of $n = 1.5$ was selected. Because the platform is not sensitive to the width, so this study proposed $w_A = w_B = 8$ mm as constant parameters.

In this study, the differential evolution (DE) algorithm was used for solving the continuous design variable optimization problems. It is a powerful technique proposed by Storn and Price (1995). With a randomly generated initial population, the DE algorithm proceeds in a step-by-step process, including mutation, crossover and selection operators. It discovers the best candidate solutions iteratively until the stopping criterion is satisfied. The following parameters were established for the DE algorithm: an initial population size of 20, and 100 epochs. The programming for the multi-objective optimization problem based on the DE algorithm in this study was executed in Matlab R2014. The optimal results, given in Table 4, show that the optimal parameters of the platform could be searched efficiently using the differential evolution algorithm. The deviation between the predicted results and the experimental validations was less than 6 %. The developed compliant micro-positioning platform had a range of motion of 860 µm and a high frequency of 345.2 Hz, see Table 5.

A fatigue analysis was necessary in the design phase of the platform. To produce the desired range of motion along the y-axis of 860 µm, the fatigue life of the platform was predicted by an FEA simulation. The stress life analysis was conducted by constructing a model from the optimal dimensions and applying a fully reversed load of 10 N. The FEA results predicted the maximum number of fatigue life cycles to be about 5.67×10^7 before the fatigue failure of the structure. Thus, the platform exhibited an approximately infinite life for producing a 860 µm range of motion.

Table 4 Optimal results

Parameters	Optimal results	Experimental validations	Error (%)
l_A (mm)	20	20	
t_A (mm)	0.6	0.6	
l_B (mm)	30	30	
t_B (mm)	0.8	0.8	
F_{CMPP} (Hz)	328.7	345.2	4.7
δ_{CMPP} (µm)	810	860	5.8

Table 5 Motion range comparison of different micro-positioning stages

Micro-positioning stages	Range of motion (µm)
The CMPP in this paper	860
Ref. (The PI Online-Catalog)	100
Ref. (Rong et al. 1994)	100
Ref. (Yang et al. 1996)	200
Ref. (Li et al. 2014)	156

The analysis results of the equivalent stress indicated that the proposed micro-positioning stage achieves the large range of motion of 860 μm with the maximum von Mises stress of 89.272 MPa without material failure (i.e., this maximum stress was still much less than the yield strength 435 MPa of Al 7075). Thus, the proposed micro-stage possesses a good performance for the micro manipulations.

For any compliant micro-positioning platform, a large displacement is one of the most significantly quality characteristics. Most previous platforms regarded how to make a large displacement or range of motion. After the optimization process, the range of motion of the CMPP was compared with that of previous platforms in the literature review. As seen in Table 5, the range of motion of the CMPP was about 8.6 times much larger than that of the commercial platform in Ref. (The PI Online-Catalog), 8.6 times higher than that of previous platform proposed by Rong et al. 1994, approximately 4.3 times greater than that of platform developed by Yang et al. 1996, and about 5.5 times larger than that of recent platform designed by Li et al. 2014. Taking advantage of a large range of motion in account, it could be concluded that the proposed CMPP is helpful for future applications, e.g., micro-positioning manipulations, microindentation and microscratch testing, as well as in situ micromechanical testing.

5 Sensitivity of developed displacement sensor

The optimal dimensions of the platform were used to determine the sensitivity of the developed strain gauge sensor. The voltage signals of 1, 2 and 3 V were applied to the piezoelectric actuator. The laser displacement sensor was adjusted to an appropriate location to achieve the most accurate displacement. The output voltage was recorded by a digital multimeter.

Using the optimal dimensions, the prototypes were manufactured; the measured average sensitivity of the developed sensor was about 0.01985. In addition, Eq. (10) predicted a sensitivity of the developed sensor of about 0.01863. Compared with the analytical prediction, the experimental result was overestimated by 4.3 %. The error came from the manufacturing and measuring tolerances, and the difference between the real and nominal strain gauge factor. It could be concluded that the developed displacement sensor can directly measure the displacement of the platform.

6 Conclusions

A compliant micro-positioning platform has developed in this paper. The platform was embedded with the strain gauges and the PDMS viscoelastic damper. The strain gauges were glued on the surfaces of the flexure hinges to form a displacement measuring sensor. The open cavities were filled with PDMS. Then the working principle of the developed gauge sensor was established.

Many FEA results showed that the length and the thickness are strongest effect on the strain and stress. In contrast, the strain and stress were not sensitive to changes in the width. And so the best positions for attaching the strain gauges were exactly determined. Two case studies without the damper and with the embedded damper were conducted along the x-axis and y-axis, respectively. The results indicated that cases the strain, displacement, first natural frequency and the stiffness without the damper are lower than those with the damper. It could be concluded that the stiffness of the platform is reinforced by the PDMS and as a result, the frequency of the platform is increased.

In addition, the dynamic model of the platform was established using the Lagrange principle. And then, the design parameters were optimized using the differential evolution algorithm to simultaneously maximize the frequency and range of motion. The results revealed that the platform possesses a high frequency of 345.2 Hz and a large range of motion of 860 μm with an infinite fatigue-life cycle of 5.67×10^7. The sensitivity of the developed sensor was determined by the calibrations and the analytical model with an error of 4.3 %. It revealed that the platform is capable of realizing the displacement measurement via the embedded strain gauge. The platform has potential applications in micro-positioning manipulations, microindentation and microscratch testing, as well as in situ micromechanical testing. In the future work, a much smaller compliant micro-positioning platform will be developed by the proposed technology, which will have a big impact on many applications.

Acknowledgments The authors acknowledge and thank the Ministry of Science and Technology of the Republic of China for their partial financial support of this study under Contact Number: MOST 104-2221-E-151-010.

Compliance with ethical standards

Conflict of interest The authors declare that they have no conflict of interest.

References

Choi KB, Lim HJ, Kim GH, Lee JJ (2014) A flexure-based scanner for a fully bidirectional operation driven by a differential piezo force. Proc Inst Mech Eng C J Mech Eng Sci 228:3186–3199. doi:10.1177/0954406214525602

Dao TP, Huang SC (2015a) Robust design for a flexible bearing with 1-DOF translation using the Taguchi method and the utility concept. J Mech Sci Technol 29(8):3309–3320. doi:10.1007/s12206-015-0728-3

Dao TP, Huang SC (2015b) Design, fabrication, and predictive model of a 1-DOF translational, flexible bearing for high precision mechanism. Trans Can Soc Mech Eng 39(3):419–429

Ghisleni R, Malyska KR, Philippe L, Schwaller P, Michler J (2009) In situ SEM indentation experiments: instruments, methodology, and applications. Microsc Res Techniq 72:242–249. doi:10.1002/jemt.20677

Guo Z, Tian Y, Liu C, Wang F, Liu X, Shirinzadeh B, Zhang D (2015) Design and control methodology of a 3-dof flexure-based mechanism for micro/nano-positioning. Robot Comput Integr Manuf 32:93–105. doi:10.1016/j.rcim.2014.10.003

Howell LL (2001) Compliant mechanisms. Wiley, New York

Huang J, Li Y (2010) Design and analysis of a completely decoupled compliant parallel XY micro-motion stage. Proceedings of the 2010 IEEE international conference on robotics and biomimetics, Tianjin, China, 1008–1013. doi:10.1109/ROBIO.2010.5723464

Huang H, Zhao H, Shi C, Wu B, Fan Z, Wan S, Geng C (2012) Effect of residual chips on the material removal process of the bulk metallic glass studied by in situ scratch testing inside the scanning electron microscope. AIP Adv 2:042193–042200. doi:10.1063/1.4774032

Huang BW, Kuang JH, Tseng JG, Wang JC, Qiu YX (2015) Seismic analysis of a viscoelastic damping isolator. Adv Mater Sci Eng 280625:1–6. doi:10.1155/2015/280625

Li Y, Xu Q (2011) A novel piezoactuated XY stage with parallel, and stacked flexure structure for micro-/nanopositioning. IEEE Trans Industr Electron 58:3601–3615. doi:10.1109/TIE.2010.2084972

Li Y, Huang J, Tang HA (2012) Compliant parallel XY micromotion stage with complete kinematic decoupling. IEEE Trans Autom Sci Eng 9:538–553. doi:10.1109/TASE.2012.2198466

Li Y, Xiao S, Xi L, Wu Z (2014) Design, modeling, control and experiment for a 2-DOF compliant micro-motion stage. Int J Precis Eng Manuf 15(4):735–744. doi:10.1007/s12541-014-0394-x

Lin HR, Cheng CH, Hung SK (2015) Design and quasi-static characteristics study on a planar piezoelectric nanopositioner with ultralow parasitic rotation. Mechatronics 31:180–188

Malyskaa KAR, Buerkia G, Michlera J, Majora RC, Cyrankowskia E, Asifa SAS, Warrena OL (2008) In situ mechanical observations during nanoindentation inside a high-resolution scanning electron microscope. J Mater Res 23:1973–1979. doi:10.1557/JMR.2008.0240

Miller JA, Hocken R, Smith ST, Harb S (1996) X-ray calibrated tunneling system utilizing a dimensionally stable nanometer positioner. Precis Eng 18:95–102. doi:10.1016/0141-6359(96)00037-2

Mukhopadhyay D, Dong J, Pengwang E, Ferreira PM (2008) A SOI-MEMS-based 3-dof planar parallel kinematics nanopositioning stage. Sens Actuators A Phys. 147:340–351. doi:10.1016/j.sna.2008.04.018

Park J, Kwon K, Bang J (2007) Development of a precision indentation and scratching system with a tool force and displacement control module. Rev Sci Instrum 78:045102. doi:10.1063/1.2719622

Polit S, Dong J (2009) Design of high-bandwidth high-precision flexure based nanopositioning modules. J Manuf Syst 28:71–77. doi:10.1016/j.jmsy.2010.01.001

Rabe R, Breguet JM, Schwaller P, Stauss S, Haug FJ, Patscheider J, Michler J (2004) Observation of fracture and plastic deformation during indentation and scratching inside the scanning electron microscope. Thin Solid Films 469–470:206–213. doi:10.1016/j.tsf.2004.08.096

Rong YM, Zhu YX, Luo ZB, Liu XX (1994) Design and analysis of flexure-hinge mechanism used in micro-positioning stages. ASME Production Engineering Division. 68:979–985

Shakoor RI, Srinivasan P, Bazaz SA (2011) Performance of a compliant structure for a thermal resonant microgyroscope. IEEE Sens J 11:1465–1475. doi:10.1109/JSEN.2010.2094185

Shigley JE, Mischke CR (1989) Mechanical engineering design. McGraw-Hill International Editions, New York, USA

Shimamoto A, Tanaka K (1997) Development of a depth controlling nanoindentation tester with subnanometer depth and submicro-newton load resolutions. Rev Sci Instrum 68:3494–3503. doi:10.1063/1.1148313

Shiou FJ, Chen CJ, Chiang CJ (2010) Development of a real-time closed-loop micro-/nanopositioning system embedded with a capacitive sensor. Meas Sci Technol 21:054007. doi:10.1088/0957-0233/21/5/054007

Smith ST, Chetwynd DG, Bowen DK (1987) Design and assessment of monolithic high precision translation mechanisms. J Phys E Sci Instrum 20:977–983. doi:10.1088/0022-3735/20/8/005

Storn R, Price K (1995) Differential evolution-a simple and efficient adaptive scheme for global optimization over continuous spaces. Int Comput Sci Instit. Technical report

Tang H, Li Y (2013) Design, analysis, and test of a novel 2-dof nanopositioning system driven by dual mode. IEEE Trans Rob 29:650–662. doi:10.1109/TRO.2013.2248536

Teo TJ, Yang G, Chen IM (2014) A large deflection and high payload flexure-based parallel manipulator for UV nanoimprint lithography: part I. modeling and analyses. Precis Eng 38:861–871. doi:10.1016/j.precisioneng.2014.05.003

The PI Online-Catalog, Physik Instrumente. http://www.physikinstrumente.com/. Accessed 10 Mar 2016

Tian Y, Liu X, Zhang D, Chetwynd DG (2009) Dynamic modeling of the fidelity of random surface measurement by the stylus method. Wear 266:555–559. doi:10.1016/j.wear.2008.04.061

Tsai CC, Lin SC, Huang HC, Cheng YM (2009) Design and control of a brushless DC limited-angle torque motor with its application to fuel control of small-scale gas turbine engines. Mechatronics 19:29–41. doi:10.1016/j.mechatronics.2008.07.003

Wang Z, Hu H (2005) Analysis and optimization of a compliant mechanism-based digital force/weight sensor. IEEE Sens J 5:1243–1250. doi:10.1109/JSEN.2005.859286

Warren OL, Asif SAS, Cyrankowski E, Kounev K (2010) Actuatable capacitive transducer for quantitative nanoindentation combined with transmission electron microscope. US Patent 7798011

Xi X, Clancy T, Wu X, Sun Y, Liu X (2016) A MEMS XY-stage integrating compliant mechanism for nanopositioning at sub-nanometer resolution. J Micromech Microeng 26:025014. doi:10.1088/0960-1317/26/2/025014

Yang R, Jouaneh M, Schweizer R (1996) Design and characterization of a low-profile micropositioning stage. Precis Eng 18:20–29. doi:10.1016/0141-6359(95)00032-1

Zubir MNM, Shirinzadeh B (2009) Development of a high precision flexure based microgripper. Precis Eng 33:362–370. doi:10.1016/j.precisioneng.2008.10.003